Isolation and Characterization of Single and Sulfide-Bridged Double [4Fe–4S] Cubane Clusters with 4-Pyridinethiolato Ligands

Deidra L. Gerlach,[a] Dimitri Coucouvanis,*[a] Jeff Kampf,[a] and Nicolai Lehnert*[a]

Cuboidal iron–sulfur clusters, [4Fe–4S], are important electron-transfer (ET) sites in biology. In addition, more complex structures, usually consisting of modified or fused cubane clusters, are used as active sites in many important enzymes. For example, the Fe–Mo cofactor (FeMoco) of nitrogenase contains two fused cubanes. Here, we report the synthesis of three new *para*-pyridylthiolate ligated iron–sulfur cubane clusters, two single clusters $(Bu_4N)_2[Fe_4S_4(SMePy)_4]$ and $(Bu_4N)_2[Fe_4S_4(SPy)_4]$, and the sulfide-bridged double cubane $(Bu_4N)_4[\{Fe_4S_4(SPy)_3\}_2S]$ with 4-pyridinethiolato exogenous ligands. The properties of these clusters were then explored by ^1H NMR, IR, and UV/Vis spectroscopy, cyclic voltammetry (CV), and X-ray crystallography. Importantly, $(Bu_4N)_4[\{Fe_4S_4(SPy)_3\}_2S]$ is the first example of a crystallographically characterized sulfide-bridged double cubane with all-thiolato exogenous ligands that is not supported by a large encapsulating ligand. This cluster shows a bridging Fe–S–Fe angle of 104°, its other structural parameters are in close agreement with those of the single-cluster analog $(Bu_4N)_2[Fe_4S_4(SPy)_4]$. Finally, the one-electron-reduced forms of $(Bu_4N)_2[Fe_4S_4(SPy)_4]$ and $(Bu_4N)_4[\{Fe_4S_4(SPy)_3\}_2S]$ were studied by low-temperature electron paramagnetic resonance (EPR) spectroscopy. Both clusters exhibit reversible one-electron reductions at –401 and –528 mV [vs. the normal hydrogen electrode (NHE)], respectively. The one-electron-reduced forms of both clusters show $S = 1/2$ ground states as evident from EPR spectroscopy at liquid-helium temperature. The temperature-dependent data for the double cubane further indicate that the extra electron is trapped in one of the clusters of the dimer and that a low-lying excited state is likely present in this complex, close in energy to the ground state.

Introduction

Iron, as the most abundant transition metal in living organisms, is utilized by biological systems for various vital processes, which take advantage of the easily accessible multiple oxidation states of iron.[1] Non-heme iron largely exists as varying forms of iron–sulfur clusters commonly ligated directly to proteins through cysteine, histidine, or aspartate side chains. In addition to the single iron center in rubredoxin, iron–sulfur clusters are widely utilized in electron-transport chains that lead to the catalytic sites of enzymes. The iron–sulfur cluster dimers, [2Fe–2S], and cubanes, [4Fe–4S], are ferredoxins that serve as one-electron reductants or oxidants. The individual iron centers in rubredoxin and the ferredoxins are essentially tetrahedrally coordinated with typical internal and external Fe–S bond lengths of 2.2–2.4 Å (Scheme 1, left and middle).[2] In the [2Fe–2S] and [4Fe–4S] ferredoxins, inorganic sulfide ions bridge the iron centers. Ligation is completed by additional cysteinate ligands.

Iron–sulfur clusters are the most widely used electron-transfer centers in biology. The versatility of use and ability to tune the reduction potentials of the ferredoxins are instrumental to the biological functions of these electron-transfer centers (Scheme 2). The single-iron-center rubredoxins have a typical redox range of 0 to –100 mV vs. the normal hydrogen electrode (NHE) for the Fe^{3+}/Fe^{2+} couple. The [2Fe–2S] ferredoxins typically operate in the range –150 to –450 mV and cycle between the $[Fe_2S_2]^{2+}/[Fe_2S_2]^+$ oxidation states.[1a] An excellent example of the tuning of the reduction potentials of iron–sulfur clusters are the [2Fe–2S] ferredoxins in comparison to the Rieske centers, which differ from the [2Fe–2S] ferredoxins in that the Rieske centers have two cysteinates ligated to one of the iron atoms and two histidines bound to the other iron center (instead of all cysteinate ligands). The reduction potentials at which the Rieske centers operate are significantly more positive (in the range –100 to +400 mV) for the $[Fe_2S_2]^{3+}/[Fe_2S_2]^{2+}$ couple compared to those of the analogous ferredoxins.[1a] The cuboidal iron–sulfur clusters are capable of operation in both the high- and low-potential ranges as observed for the [2Fe–2S] dimers. This again is an example of the ability of

[a] Department of Chemistry, University of Michigan,
930 N University, Ann Arbor, MI 48109
E-mail: lehnertn@umich.edu,
www.umich.edu/~lehnert/

WILEY
ONLINE LIBRARY
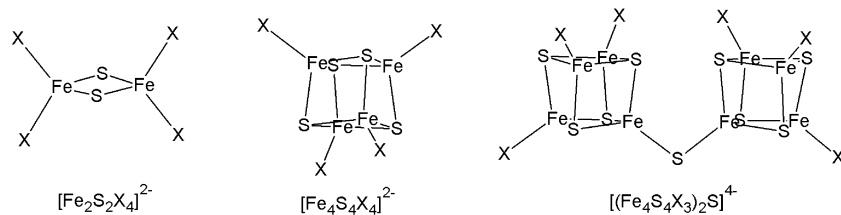
Scheme 1. Structures of the iron–sulfur dimer cluster $[Fe_2S_2X_4]^{2-}$ (left), cubane cluster $[Fe_4S_4X_4]^{2-}$ (middle), and sulfide-bridged double cubane cluster $[(Fe_4S_4X_3)_2S]^{4-}$ (right). "X" is an appropriate anion such as $^-$S-(Cys) in ferredoxins and halides or thiolates in synthetic iron–sulfur clusters.
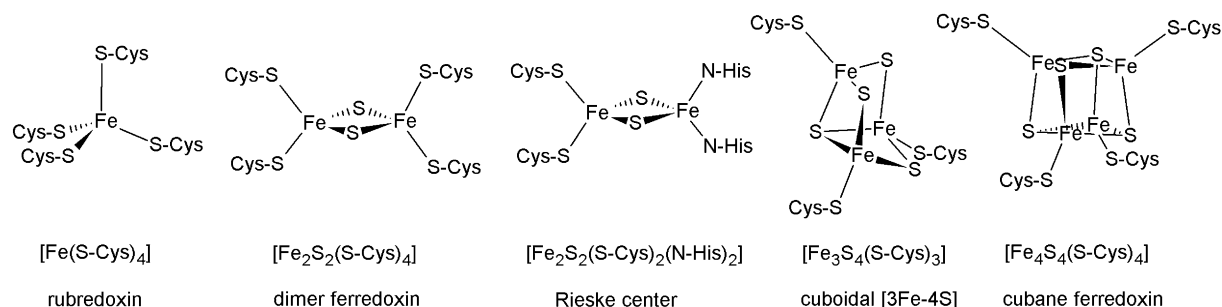

Scheme 2. Protein active-site structures of typical iron–sulfur clusters.

biology to modify and fine-tune redox potentials of iron–sulfur clusters. Most cuboidal ferredoxins transfer electrons in the range –300 to –700 mV for the $[Fe_4S_4]^{2+}/[Fe_4S_4]^{1+}$ couple. However, adjustments in the protein environment allowing for different degrees of solvation stabilize the clusters in the higher oxidation state and allow operation at more positive potentials of +100 to +400 mV by using the $[Fe_4S_4]^{3+}/[Fe_4S_4]^{2+}$ couple.[1a,3] These sites are usually referred to as high-potential iron proteins (HiPIPs).

The thermodynamic stability of the ferredoxins allows for self-assembly syntheses of clusters of the types $[Fe_4S_4(SR)_4]^{2-}$ and $[Fe_4S_4X_4]^{2-}$ in one-pot reactions from ferric chloride, sulfide, a strong base, and mercaptans.[4] The lability of the exogenous ligands of the iron–sulfur clusters in polar coordinating solvents allows for easy ligand exchange for the rational synthesis of clusters with desired properties and structures. Previous publications on iron–sulfur clusters have reported a large variety of thiolate (–SR) clusters synthesized by this method, including those with aliphatic and aromatic R groups that incorporate electron-withdrawing and -donating groups, various degrees of side chain lengths and branching, peptides, dendrimer thiolates, di- and trithiolates, and site-differentiating thiolate ligands.[2] Other strong σ donor ligands such as phenolates, halides, amines, cyanide, amides, phosphanes, and crown ethers have also been used as ligands for [4Fe–4S] clusters.[2,4a,5] A recent publication from the Holm group explores the use of β-cyclodextrin dithiolate ligands to afford water-soluble, stable [4Fe–4S] clusters.[6] Thiol exchange of pyridinethiolato ligands with [4Fe–4S] clusters, as applied here, has been published by Mochida and co-workers with focus on ortho-pyridinethiolato as a bidentate ligand.[7]

As previously shown, the addition of sulfide to synthetic [4Fe–4S] clusters results in singly μ-sulfido-bridged double cubane clusters (Scheme 1, right). The crystal structures of these clusters are highly pursued to aid in the structural elucidation and biomimetic synthesis of models of the (Mo/Fe)Fe cofactor and P-cluster of nitrogenase.[8] Although spectroscopic evidence has previously shown that sulfide-bridged double cubanes do form, only three crystal structures of sulfide-bridged cubane clusters have been published to date.[5b,9] The first structure was reported by Challen from the Coucouvanis group and was obtained for the all-chloro cubane by using mixed counterions.[9b] Recently, two sulfide-bridged cubane clusters ligated by newly reported encapsulating ligands, Temp(SH)$_3$ and Tefp(SH)$_3$, were prepared and structurally characterized by the Tatsumi group (Scheme 3).[9d] Each one of these sulfide-bridged clusters is unique within a range of Fe–S–Fe bond angles for the bridge and rotations of the iron–sulfur cubanes with respect to each other. The all-chloro bridged cubane of Challen is the most symmetrical and has C_{2v} symmetry. On the other hand, the bridged cluster of Tatsumi with the TefpS$_3$ encapsulating ligand has a near-linear (and disordered) sulfide bridge between the two clusters. It is not clear whether it is the polarity of the para group of the phenylthiolate of the encapsulating ligand or if it is the crystal packing that is responsible for the large effect on the bond angle for these complexes in the solid state. Further analysis is provided below in the Results and Discussion section.

In this paper, we report the synthesis and characterization of two new iron–sulfur clusters coordinated by para-substituted pyridylthiolate-type ligands, (Bu$_4$N)$_2$[Fe$_4$S$_4$(SPy)$_4$] and (Bu$_4$N)$_2$[Fe$_4$S$_4$(SMePy)$_4$], which are ligated by
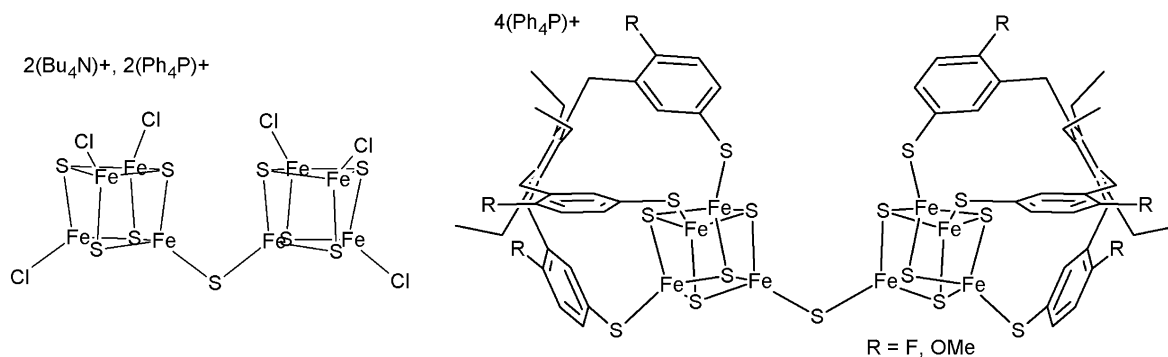
Scheme 3. Structures of previously published sulfide-bridged [4Fe–4S] cubane clusters: $(Bu_4N)_2(Ph_4P)_2[(Fe_4S_4Cl_3)_2S]$ (left)[9b] and $(Ph_4P)_4$-$[\{Fe_4S_4(TempS_3)\}_2S]$ (R = OMe) and $(Ph_4P)_4[\{Fe_4S_4(TefpS_3)\}_2S]$ (R = F, right).[9d]

the 4-pyridinethiolato (−SPy) and 4-pyridinemethanethiolato (−SMePy) ligands, respectively. Excitingly, we also present the fourth crystal structure of a sulfide-bridged cubane cluster with 4-pyridinethiolato as the exogenous ligand, $(Bu_4N)_4[\{Fe_4S_4(SPy)_3\}_2S]$. Finally, we report the properties of the one-electron-reduced sulfide-bridged cubane cluster as determined by electron paramagnetic resonance (EPR) spectroscopy.

Results and Discussion

Cluster Syntheses

The precursor iron–sulfur cubane cluster $[Fe_4S_4(SEt)_4]^{2-}$ with exogenous ethanethiolato ligands is easily prepared in a one-pot, self-assembly reaction under anaerobic conditions.[4a] From the straightforwardly obtained tetraethanethiolate cubane cluster, thiol exchange is often readily accomplished by the addition of an acidic thiol. Here, the acidic thiol will transfer the thiol proton to the ethanethiolato ligand in polar solvents, in which the ethanethiolato ligand is labile. The highly volatile ethanethiol is readily removed under vacuum, which allows the direct ligation of the introduced thiol to the iron–sulfur cluster. This synthetic route works well with 4-pyridinemethanethiol and evidently occurs for 4-pyridinethiol as well to produce the clusters $(Bu_4N)_2[Fe_4S_4(SMePy)_4]$ and $(Bu_4N)_2[Fe_4S_4(SPy)_4]$, respectively. However, in the presence of just 4-pyridinethiol without added sulfide, free sulfide is also liberated from the cubanes in solution; this indicates that decomposition of some of the iron–sulfur clusters aided by ligation to 4-pyridinethiol also occurs, which is quite unusual. Importantly, it has been shown previously that in polar solvents, particularly protic solvents, the tautomerization of 4-pyridinethiol to 4-pyridylthione readily occurs with strong preference for the thione (Scheme 4).[10] Hence, most of the pyridinethiol is in the thione form in the reaction mixture with acetonitrile as the solvent. The presence of the pyridylthione in solution apparently destabilizes the cluster, possibly because the increased acidity of the pyridyl group over the thiol leads to the liberation of sulfide ions from the iron–sulfur cluster core. As a result, a mixture of the single cubane and the singly sulfide-bridged double cubane $(Bu_4N)_4$-

$[\{Fe_4S_4(SPy)_3\}_2S]$ is formed in solution and appears to be in equilibrium in polar solvents. For example, when the pure single cubane is recrystallized, a minor fraction of the precipitated solid is identified as the sulfide-bridged double cubane cluster generated in the recrystallization process. In reactions in which free sulfide ions are introduced as the sodium salt, the concentration of the sulfide-bridged iron–sulfur cubane increases to become the major cubane cluster in solution, although a minor fraction of the single cubane is also generated in the synthesis. In contrast, no cluster decomposition and formation of double cubanes is observed with 4-pyridinemethanethiol, which provides further support to the idea that the decomposition is linked to the tautomerization of 4-pyridinethiol. Scheme 5 shows the syntheses of these iron–sulfur clusters.
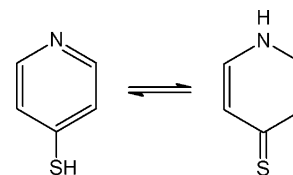
Scheme 4. The tautomerization of 4-pyridinethiol to 4-pyridylthione.

Unfortunately, the similarity in polarity of the single and double cubane clusters with 4-pyridinethiolato ligands and, thus, their similar solubility makes separation by crystallization nearly impossible. Chromatography has not been a viable means for separation of these clusters either, as most separation media either irreversibly trap the clusters or decompose the clusters. Successful individual crystallization of the single cubane cluster and the singly sulfide-bridged double cubane was achieved by slow diffusion of diethyl ether into acetonitrile solutions of the cluster mixtures. Separation was only possible by physical (manual) separation of individual crystals of the two iron–sulfur clusters in the recrystallization batches. The single cubane crystallizes as square and rectangular block crystals, whereas the singly sulfide-bridged double cubane crystallizes as thin rodlike crystals and larger thin plate crystals. Most often, both clusters precipitate as powder together or crystallize partially as the other cluster deposits on the growing crystals. The ability to distinguish the crystals of the pure cubane clusters
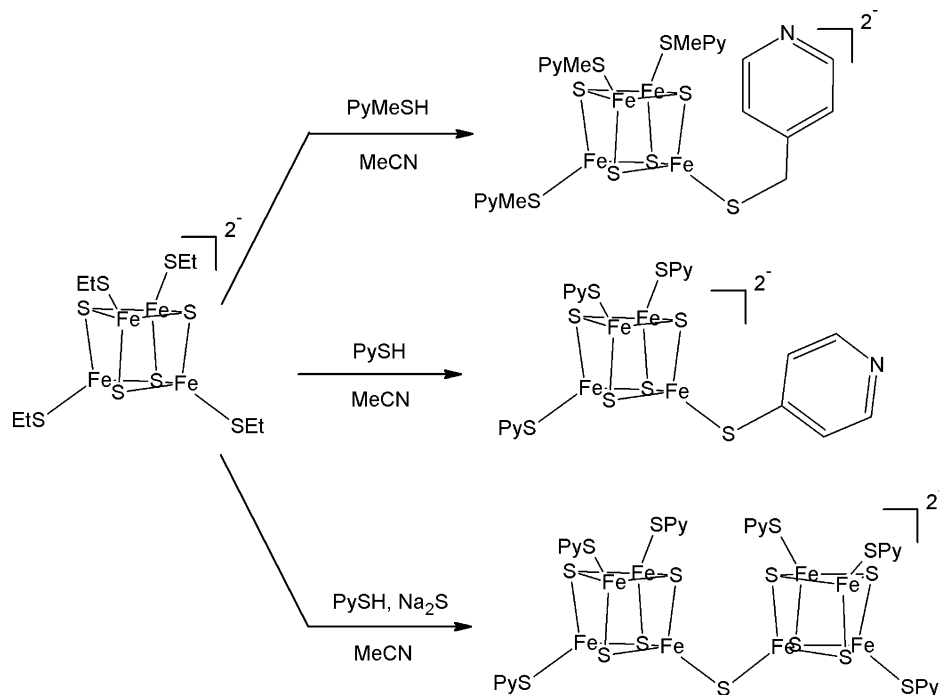
Scheme 5. Synthesis of $(Bu_4N)_2[Fe_4S_4(SMePy)_4]$ (top right), $(Bu_4N)_2[Fe_4S_4(SPy)_4]$ (middle right), and $(Bu_4N)_4[\{Fe_4S_4(SPy)_3\}_2S]$ (bottom right). In the two latter cases, the major products of the reaction are indicated.

from each other by eye and to grow larger crystals permits physical separation of the crystals by hand with a needle and static. Milligrams of crystals can be collected over a few hours of separation by this means. The purity of these collections can be easily verified by ${}^1H$ NMR spectroscopy by the unique signals of the aromatic protons of the 4-pyridinethiolato ligands (see Figures S6 and S9 for the pure compounds vs. Figure S10 for the crude material collected from a synthesis of the sulfide-bridged double cubane). Owing to the added steric hindrance in the sulfide-bridged double cubane, the free rotation of the pyridine rings about the iron thiolate sulfur bonds as well as the rotation of the exogenous Fe–S bond of the sulfide is limited and, thus, the peak of the *ortho*-hydrogen atom at $\delta = 5.13$ ppm is sharper in the double cubane complex than the analogous peak for the single cluster ($\delta = 5.92$ ppm). In addition, the extra electron density owing to the sulfide bridge shifts the signals of the *ortho*- and *meta*-hydrogen atoms upfield and downfield ($\delta = 5.13$ and 9.15 ppm), respectively, compared to the analogous signals for $(Bu_4N)_2[Fe_4S_4(SPy)_4]$ at $\delta = 5.92$ and 8.96 ppm. This distinction of the peak positions in the ${}^1H$ NMR spectra was used to gather pure materials for further characterization.

The Fe–S stretch observed in the far-infrared region is often used as a fingerprint for iron–sulfur clusters that undergo ligand exchange. Not surprisingly, the far-IR spectra of $(Bu_4N)_2[Fe_4S_4(SPy)_4]$ and $(Bu_4N)_2[Fe_4S_4(SMePy)_4]$ (Figures S4 and S1) are similar: both exhibit the most intense signal at 356 cm^{-1}, which is relatively sharp for this spectral region and indicates a high degree of symmetry in the Fe–S bonds. In contrast, the Fe–S stretch of the sulfide-bridged cluster $(Bu_4N)_4[\{Fe_4S_4(SPy)_3\}_2S]$ at 367 cm^{-1} is broader,

and multiple shoulders are visible on the main signal, which indicates a loss of symmetry for the two bridged [4Fe–4S] clusters (Figures S4 and S7). A similar spectrum results for the sulfide-bridged cluster $(Bu_4N)_2(Ph_4P)_2[(Fe_4S_4Cl_3)_2S]$ of Challen, for which five distinct shoulders are observed on the Fe–S stretching band.[11]

Structures and Comparisons

Both the 4-pyridinethiolato-ligated single cubane and the sulfide-bridged double cubane afforded single crystals for structure determination. In each crystal structure, the [4Fe–4S] cores are conserved with geometries typical for tetrahedrally distorted iron centers of iron–sulfur cubanes with D_{3d} symmetry. The internal and external Fe–S bond lengths of the $[Fe_4S_4(SR)_x]^{2-}$ anions are on average in the 2.2–2.4 Å range with more obtuse S–Fe–S angles and more acute Fe–S–Fe angles in the $[Fe_4S_4]$ cores as is expected for typical tetrathiolate-ligated [4Fe–4S] cubane clusters. At this time, single crystals for structural determination have not been collected for our $(Bu_4N)_2[Fe_4S_4(SMePy)_4]$ cubane; however, a structure was recently published for the analogous cluster with *meta*-PyMeS${}^-$ ligands.[12]

The single cubane $(Bu_4N)_2[Fe_4S_4(SPy)_4]$ crystallizes as black cubic crystals with two unique clusters and four unique tetrabutylammonium counterions in the monoclinic $C2/c$ unit cell. Unfortunately, this structure is inherently disordered and, hence, could not be refined satisfactorily. Therefore, this structure should be considered preliminary, although the fit for the cluster anion itself is of high quality (see Supporting Information). The crystal packing shows
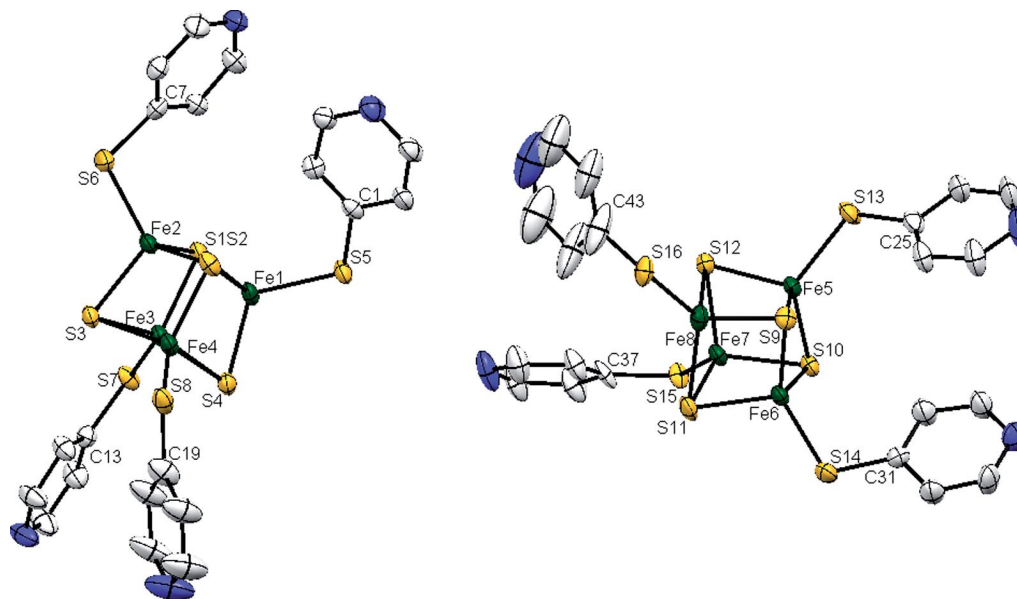
Figure 1. ORTEP diagram of the preliminary structure (see text) of $(Bu_4N)_2[(Fe_4S_4(SPy)_4]$ with disordered 4-pyridinethiolato ligands, hydrogen atoms and $(Bu_4N)^+$ counterions omitted for clarity. The structural parameters are listed in Table 1.

two alternating layers: the first one comprises three unique counterions, which are spread out laterally within the layer, and the second one contains the [4Fe–4S] clusters and one unique counterion oriented orthogonally to those in the counterion layer (Figure S13). The ORTEP diagram of the cluster anions with 50% thermal ellipsoids is shown in Figure 1 with disordered atoms, hydrogen atoms, and counterions omitted for clarity. Each one of the 4-pyridinethiolato ligands has a second position as defined in the structure in Figure S12.

The preliminary structure of $(Bu_4N)_2[Fe_4S_4(SPy)_4]$ is not at all an exception for a $[Fe_4S_4(SR)_4]^{2-}$ cubane cluster structure. With typical average bond lengths and core bond angles, the only significant differences in structure in comparison to the well-known iron–sulfur cubane $[Fe_4S_4(SPh)_4]^{2-}$ with the same tetrabutylammonium counterion lie in the rotation of the exogenous thiolate ligands (Figure 2).[13] These ligands are free to rotate and bend as is observed for the two separate cluster ions in the unit cell of $(Bu_4N)_2[Fe_4S_4(SPy)_4]$, but overall, the phenyl/pyridine residues of the ligands are oriented in a way that two ligands reach in the same direction and the other two point the opposite way (see Figure 2). The obvious difference in the crystal packing of $(Bu_4N)_2[Fe_4S_4(SPh)_4]$ and $(Bu_4N)_2[Fe_4S_4(SPy)_4]$ is that the phenylthiolate clusters all stack the same way in the solid state, whereas the pyridinethiolate clusters are rotated with respect to each other.

The sulfide-bridged double cubane crystallizes as wide, black needles. The monoclinic $P2_1/n$ unit cell of $(Bu_4N)_4-[\{Fe_4S_4(SPy)_3\}_2S]$ contains one unique complex with four unique counterions (Figure S14). The ORTEP diagram of the cluster anions with 50% thermal ellipsoids is shown in Figure 3. Here, disordered atoms, hydrogen atoms, and counterions are omitted for clarity. Remarkably, very little disorder is found in this structure. Of the six 4-pyridine-
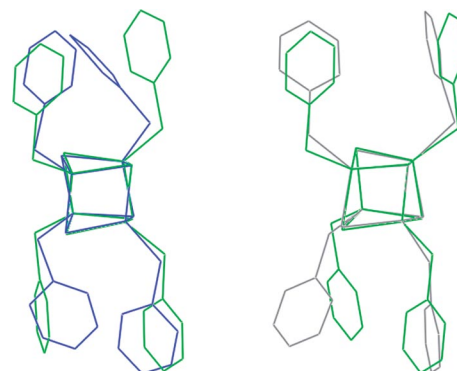

Figure 2. Wire-frame overlay of the two equivalent anions of $[Fe_4S_4(SPy)_4]^{2-}$ (blue, grey) with the $[Fe_4S_4(SPh)_4]^{2-}$ anion (green); counterions and hydrogen atoms omitted for clarity.

thiolato ligands, only two have more than one orientation, and in addition, the tetrabutylammonium counterions, which are notorious for having disordered crystal packings, are also well ordered in this structure. The usual orientation of the 4-pyridinethiolato ligands, or phenyl groups in the single $[Fe_4S_4(SR)_4]^{2-}$ clusters, is also observed here for each cubane. The only exception of this is found for the Fe4–S5–Fe5 sulfide bridge (see Figure 3). Here, for the cubane containing Fe4, the Fe4–S5–Fe5 bond angle and position is in the proper "down" position as the aromatic group would be. However, for the cubane containing Fe5, the Fe5–S5–Fe4 bond angle and position is rotated by ca. 180° from the expected position so that the Fe4 cubane "ligand" is in a "down" position when it would be expected to be in an "up" position. Steric crowding of the pyridine rings likely enforces this orientation; as seen in Figure 3, the 4-pyridinethiolato ligand with S12 and C11 is pinched between the ligands with S13 and C16 and S15 and C26, opposite
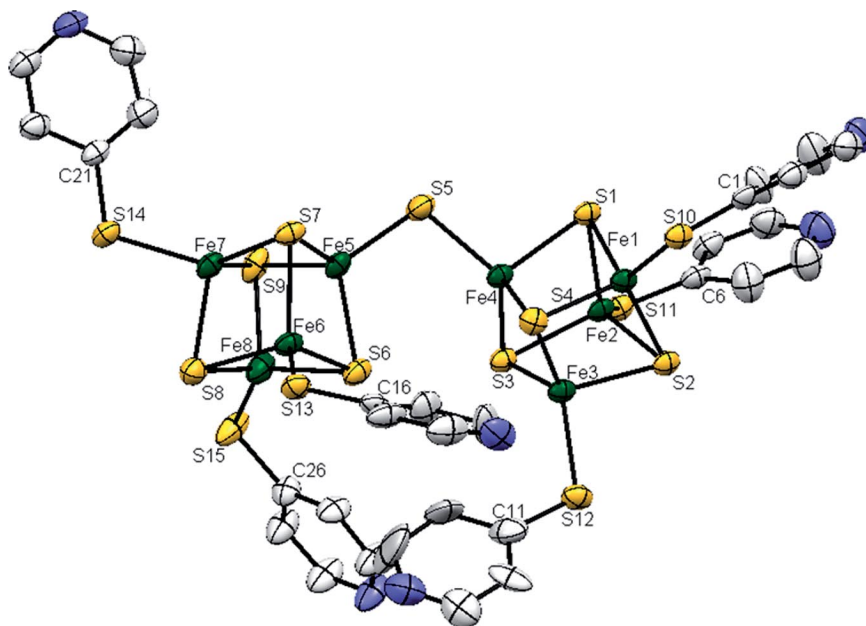
Figure 3. ORTEP diagram of $(Bu_4N)_4[\{Fe_4S_4(SPy)_3\}_2S]$ with disordered S15 and S12 4-pyridinethiolato ligands, hydrogen atoms, and $(Bu_4N)^+$ counterions omitted for clarity. The structural parameters are listed in Table 1.

the bridging sulfide atom at the center of the double cubane, which likely locks this orientation in place in the solid state. Despite these structural peculiarities in the solid state, it seems that all 4-pyridinethiolato ligands are equivalent in solution, as indicated by ^{1}H NMR spectroscopy at room temperature, which shows one broad signal for each the *meta-* and *ortho*-hydrogen atoms of the 4-pyridinethiolato ligand rings at $\delta = 9.15$ and 5.13 ppm, respectively (Figure S6 and S9).

A comparison between the bridging Fe–S and exogenous Fe–S/Cl bond lengths of $(Bu_4N)_4[\{Fe_4S_4(SPy)_3\}_2S]$ and the previously published sulfide-bridged double cubane clusters is highlighted in Table 1. These data indicate that a lengthening or shortening of typical Fe–S and Fe–Cl bonds is not observed for the exogenous ligands of the sulfide-bridged double cubane clusters. However, the bond angles show some differences between the four sulfide-bridged clusters. Whereas $(Ph_4P)_4[\{Fe_4S_4(TefpS_3)\}_2S]$ has a nearly linear Fe–S–Fe bridge, $(Bu_4N)_4[\{Fe_4S_4(SPy)_3\}_2S]$, $(Bu_4N)_2(Ph_4P)_2$-$[(Fe_4S_4Cl_3)_2S]$, and $(Ph_4P)_4[\{Fe_4S_4(TempS_3)\}_2S]$ display close to ideal tetrahedral bond angles for the bridging sulfide ion. Although $(Bu_4N)_2(Ph_4P)_2[(Fe_4S_4Cl_3)_2S]$ has the smallest bond angle, which may be caused by the effect of the polar chloride exogenous ligands on the iron–sulfur core, the steric bulk of this series of complexes is not equivalent nor is the crystal packing, so one has to be careful in

interpreting small differences in Fe–S–Fe angles. In addition, the double cubane $(Ph_4P)_4[\{Fe_4S_4(TefpS_3)\}_2S]$ with the linear bridge shows disorder in the bridging sulfide, which further complicates accurate interpretation of the Fe–S–Fe bridging angle in this compound.

A stereoview of the overlaid core structures of $(Bu_4N)_4$-$[\{Fe_4S_4(SPy)_3\}_2S]$, $(Bu_4N)_2(Ph_4P)_2[(Fe_4S_4Cl_3)_2S]$, and $(Ph_4P)_4[\{Fe_4S_4(TempS_3)\}_2S]$ is shown in Figure 4; this illustrates the "rotation" of the second [4Fe–4S] core relative to the first, which is held stationary.[9b,9d] Figure 5 presents all of the sulfide-bridged double cubanes (see Table 1). Here, the atoms of the Fe–S–Fe bridge are located in the plane of the paper such that the symmetry of each one of the complexes is highlighted. $[\{Fe_4S_4(SPy)_3\}_2S]^{4-}$, shown in Figure 5, exhibits no rotational symmetry or mirror plane connecting the two iron–sulfur cores. However, a near perfect mirror plane defined by the atoms of the bridge exists for this double cubane. Both clusters $[(Fe_4S_4Cl_3)_2S]^{4-}$ and $[\{Fe_4S_4(TempS_3)\}_2S]^{4-}$ contain a C_2 rotation axis that passes vertically through the bridging sulfide ion; this connects the iron–sulfur cores, which are slightly twisted in opposite directions from the plane defined by the three bridging atoms. Lastly, the complex $[\{Fe_4S_4(TefpS_3)\}_2S]^{4-}$ is the most symmetrical sulfide-bridged double cubane and has an inversion center that includes the entire encapsulating ligand $TefpS_3^{3-}$.

Table 1. Selected structural parameters of sulfide-bridged double cubanes.

FeS cluster	Fe–S–Fe angle (bridge) [°]	Fe–S bond length (bridging) [Å]	Fe–S(Cl) bond length (exogenous) [Å][a]	Ref.
$(Bu_4N)_4[\{Fe_4S_4(SPy)_3\}_2S]$	104.02	2.200	2.290	this work
$(Bu_4N)_2(Ph_4P)_2[(Fe_4S_4Cl_3)_2S]$	102.10	2.203	2.223	[9b]
$(Ph_4P)_4[\{Fe_4S_4(TempS_3)\}_2S]$	109.66	2.213	2.267	[9d]
$(Ph_4P)_4[\{Fe_4S_4(TefpS_3)\}_2S]$	161.72	2.143	2.267	[9d]

[a] Average.
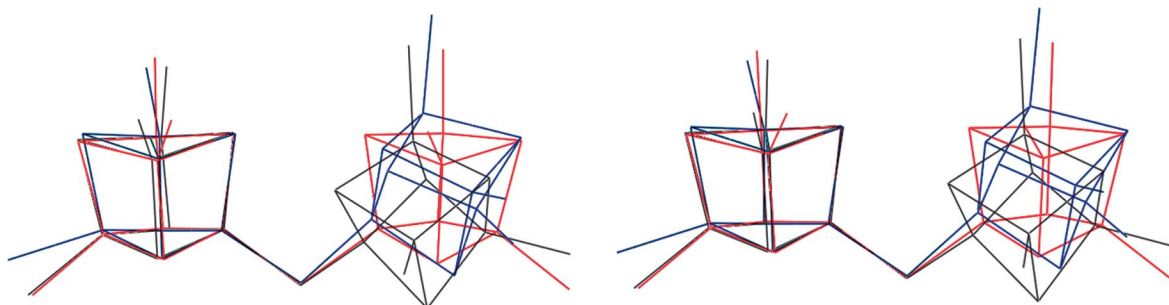
Figure 4. Stereo view of the wire-frame overlay of $[\{Fe_4S_4(SPy)_3\}_2S]^{4-}$ (blue), $[\{Fe_4S_4(Cl)_3\}_2S]^{4-}$ (grey), and $[\{Fe_4S_4(TempS_3)\}_2S]^{4-}$ (red) with counterions, aromatic rings, and solvent molecules omitted for clarity.
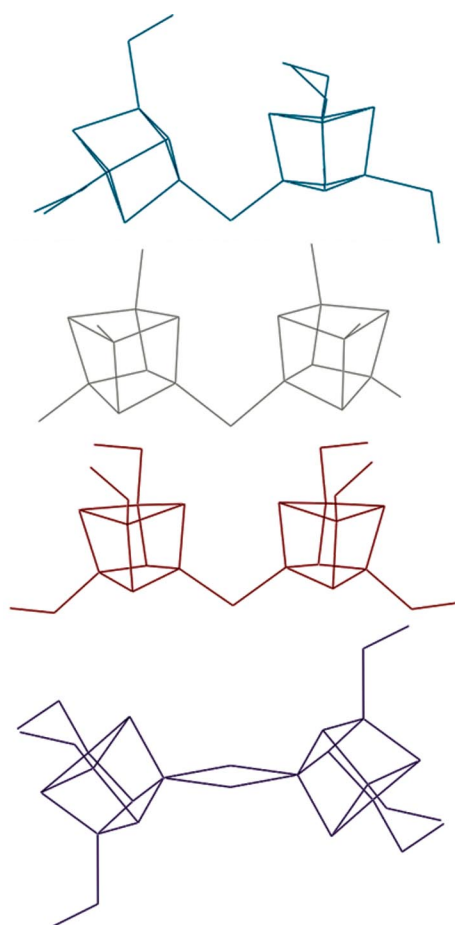

Figure 5. Wire-frame side view highlighting the sulfide-bridge angles of $[\{Fe_4S_4(SPy)_3\}_2S]^{4-}$ (top, blue), $[\{Fe_4S_4(Cl)_3\}_2S]^{4-}$ (second, grey), $[\{Fe_4S_4(TempS_3)\}_2S]^{4-}$ (third, red), and $[\{Fe_4S_4(TefpS_3)\}_2S]^{4-}$ (last, purple) with disordered ligand atoms, counterions, aromatic rings, and solvent molecules omitted for clarity.

Electrochemistry

All of the unique pyridylthiolate ligated clusters synthesized here have irreversible oxidation events at potentials of $E_{pa} \approx 400$–500 mV vs. NHE. The single cubane cluster $(Bu_4N)_2[(Fe_4S_4(SPy)_4]$ has one observable reduction event at $E_{1/2} = -401$ mV vs. NHE, whereas the $(Bu_4N)_2$-$[(Fe_4S_4(SMePy)_4]$ cluster has two observable reductions at
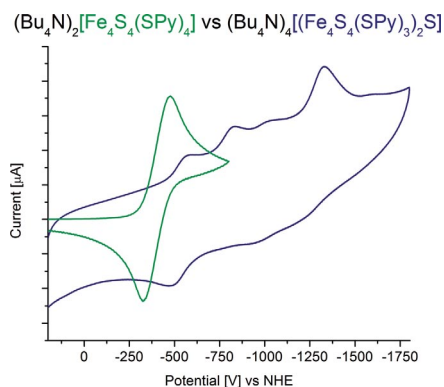
Figure 6. Cyclovoltammograms of $(Bu_4N)_2[Fe_4S_4(SPy)_4]$ (green) and $(Bu_4N)_4[\{Fe_4S_4(SPy)_3\}_2S]$ (blue) in MeCN.

$E_{1/2} = -742$ and -1459 mV (Figure 6 and S2). All of these reduction events for the single cubane clusters are essentially reversible.

In comparison to literature values for analogous single iron–sulfur clusters (see Table 2), the same trend is observed for clusters with other aromatic thiolate ligands. When converting from the short chain ethanethiolato ligand of $(Bu_4N)_2[Fe_4S_4(SEt)_4]$ to aromatic thiolates, the reduction potentials generally shift distinctively more positively from -1076 mV vs. NHE for the ethanethiolato cluster. This is expected as phenylthiolato ligands are weaker donors than alkanethiolato ligands. This effect is less pronounced for benzylthiolato ligands; for example, the benzyl clusters $(Bu_4N)_2[Fe_4S_4(SBz)_4]$ and $(Bu_4N)_2[Fe_4S_4(SMePy)_4]$ show reduction potentials of -946 and -742 mV, respectively, compared to the analogs $(Bu_4N)_2[Fe_4S_4(SPh)_4]$ and $(Bu_4N)_2$-$[Fe_4S_4(SPy)_4]$ with reduction potentials of -756 and -401 mV, respectively. This illustrates that benzylthiolato ligands have a somewhat intermediate donicity between alkane and phenylthiolato ligands, and the pyridine-based thiolato ligands applied here follow this trend well.

The sulfide-bridged double cubane $(Bu_4N)_4[\{Fe_4S_4$-$(SPy)_3\}_2S]$ has four observable reduction events with distinct E_{pc} signals and merged E_{pa} signals, so that only the first reduction event can be quantified as $E_{1/2} = -528$ mV (Figures 6 and S8). Owing to the method of hand-collecting crystals of the sulfide-bridged cluster, the concentration of the cluster in the CV experiment was quite low. Neverthe-

Table 2. $E_{1/2}$ reduction potentials of relevant single iron–sulfur clusters vs. NHE [mV] in MeCN.

FeS single cluster	$[Fe_4S_4]^{2+/1+}$	$[Fe_4S_4]^{1+/0}$	Ref.
$(Bu_4N)_2[Fe_4S_4(SEt)_4]$	–1076	–	[14]
$(Bu_4N)_2[Fe_4S_4(SPy)_4]$	–401	–	this work
$(Bu_4N)_2[Fe_4S_4(SPh)_4]$	–756	–1486	[14]
$(Bu_4N)_2[Fe_4S_4(SMePy)_4]$	–742	–1459	this work
$(Bu_4N)_2[Fe_4S_4(SBz)_4]$	–946	–	[15]

less, the signals in the cyclovoltammogram are significant enough to discern them from the background charge of the electrodes, but are too weak to allow for the identification of the E_{pa} potentials.

Each [4Fe–4S] cluster can undergo two reductions to form the all-ferrous cubane cluster; therefore, theoretically, each double cubane cluster should be able to be reduced by four electrons. All of the double cubane clusters compared here are electronically coupled through the sulfide-bridge. This is evident from the multiple one-electron reductions observed in the cyclovoltammograms for each double cubane. Rather than the reduction of each subcluster by one electron at the same potential to produce a two-electron process, both clusters are electronically coupled across the sulfide bridge, which leads to a split in the potential of the two coupled redox events. Therefore, the second reduction event is at a more negative potential and is observed as a distinct process. For both clusters $(Bu_4N)_4[\{Fe_4S_4(SPy)_3\}_2S]$ and $(Bu_4N)_2(Ph_4P)_2[(Fe_4S_4Cl_3)_2S]$, four one-electron reduction processes are identified by their cathodic peaks, whereas the corresponding anodic peaks are ill defined.[11] Three reduction events are reported for the sulfide-bridged clusters of Tatsumi; unfortunately, a comparison of the reduction potentials with those of the other clusters is impossible as the potentials are referenced vs. Ag/AgNO$_3$ of unreported concentration.[9d]

The single cluster $(Bu_4N)_2[Fe_4S_4(SPy)_4]$ is slightly easier to reduce than the sulfide-bridged double cubane $(Bu_4N)_4[\{Fe_4S_4(SPy)_3\}_2S]$ with reduction potentials of –401 and –528 mV, respectively. This order is reversed for the all-chloro single and sulfide-bridged double cubane clusters $(Bu_4N)_2[Fe_4S_4Cl_4]$ and $(Bu_4N)_2(Ph_4P)_2[(Fe_4S_4Cl_3)_2S]$, which have reduction potentials of –566 and –456 mV, respectively. In the case of the 4-pyridinethiolato-bound single and double cubane clusters, the replacement of one thiolato ligand for a sulfide ion (bound to another [4Fe–4S] cluster) makes the double cluster more difficult to reduce with a more negative reduction potential (here, the average potential of the first two reduction events of the double cubane

should actually be used for comparison); this indicates that the $^-$S–[4Fe–4S] ligand is a distinctively stronger donor than the 4-pyridinethiolato ligand. On the other hand, the chloride ligand is a stronger donor and, thus, the replacement of one chloride ligand in the corresponding double cubane leaves the (average) potential essentially unchanged compared to the first reduction potential of the all-chloro single cubane. The reduction potentials of the sulfide-bridged clusters are summarized in Table 3.

EPR Spectroscopy of One-Electron-Reduced Clusters

Each cubane cluster in the $[Fe_4S_4]^{2+}$ state has two ferric and two ferrous iron atoms; a face of the cubane contains a high-spin Fe^{3+} ion and a high-spin Fe^{2+} ion ferromagnetically coupled for a combined spin of $S = 9/2$. The two opposite faces of the cubane are antiferromagnetically coupled, which results in the total spin of $S = 0$.[4b] The 4-pyridinethiolato-ligated cubane clusters synthesized here gave no EPR signals in their isolated state in agreement with this. To prepare the one-electron-reduced cubanes, solutions of the tetrabutylammonium salts of $[(Fe_4S_4(SPy)_4]^{2-}$ and $[\{Fe_4S_4(SPy)_3\}_2S]^{4-}$ were reduced with sodium acenaphthylene in the presence of Bu_4NBr and subsequently frozen. The resulting reduced clusters $[(Fe_4S_4(SPy)_4]^{3-}$ and $[\{Fe_4S_4(SPy)_3\}_2S]^{5-}$ each exhibit an EPR sig-
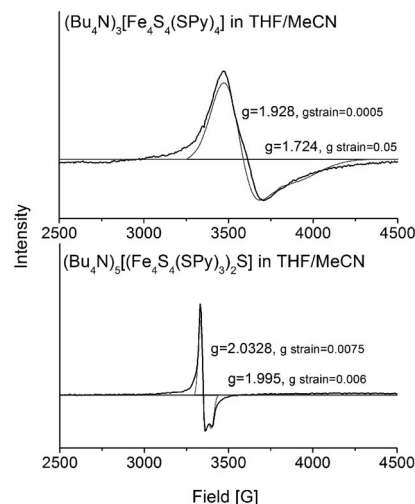
Figure 7. EPR spectra of the one-electron-reduced clusters $(Bu_4N)_3[Fe_4S_4(SPy)_4]$ (top) and $(Bu_4N)_5[\{Fe_4S_4(SPy)_3\}_2S]$ (bottom) at 4.3 K. The colored lines are the simulated spectra obtained by using the program Spin Count (M. Hendrich, Carnegie Mellon University).

Table 3. Reduction potentials of relevant sulfide-bridged iron–sulfur clusters vs. NHE [mV] in MeCN.

Sulfide-bridged FeS cluster	$[(Fe_4S_4)_2S]^n$				Ref.
	n = 4+/3+	n = 3+/2+	n = 2+/1+	n = 1+/0	
$(Bu_4N)_4[\{Fe_4S_4(SPy)_3\}_2S]$	–528	–828[b]	ca. –1050[b]	ca. –1370[b]	this work
$(Bu_4N)_2(Ph_4P)_2[(Fe_4S_4Cl_3)_2S]$	–456	–776	ca. –1156[b]	–	[9b,11]
$(Ph_4P)_4[(Fe_4S_4(TempS)_3)_2S]^{[a]}$	(–1660)	(–1870)	(–2310)[b]	–	[9d]
$(Ph_4P)_4[(Fe_4S_4(TefpS)_3)_2S]^{[a]}$	(–1550)	(–1740)	(–2240)[b]	–	[9d]

[a] Referenced vs. Ag/AgNO$_3$ of unreported concentration. [b] E_{pc} value as E_{pa} is undefined.

nal that corresponds to an axial $S = 1/2$ ground state that results from the simple addition of the unpaired electron spin to the starting $S = 0$ states (Figure 7). The $S = 1/2$ EPR signal of the reduced single cluster $(Bu_4N)_3[(Fe_4S_4(SPy)_4]$ decreases in intensity significantly when the sample is warmed above 8 K and has axial g values of $g_x = g_y = 1.928$ and $g_z = 1.724$. It should be noted that $g < 2$ is not uncommon for ferredoxins owing to antiferromagnetic coupling of Fe^{2+} and Fe^{3+} ions as described in the Heisenberg–Dirac–van Vleck Hamiltonian.[4b] In the case of the bridged double cubane, the one-electron-reduced state corresponds to a mixed-valent compound, but not of two bridged metal centers, which is the usual case, but of two linked clusters: $[Fe_4S_4]^+$–S–$[Fe_4S_4]^{2+}$. The extra electron could be localized on one cluster, oscillate between the clusters, or could be quantum-mechanically delocalized. However, at the same time, the extra electron is also delocalized within one cluster. This creates an interesting electronic situation. When the sample of the double cubane cluster is warmed above 8 K, the intensity of the $S = 1/2$ signal has an initial decrease, then increases at ca. 45 K, and finally decreases again as shown in Figure 8. The sharp axial EPR signal of $(Bu_4N)_5[\{Fe_4S_4(SPy)_3\}_2S]$ has g values of $g_x = g_y = 2.0328$

and $g_z = 1.995$, in contrast to the rhombic g values reported by Holm and co-workers for double cubanes bridged by small organic dithiolates.[9a] Over the whole temperature range (see Figure 8), no broadening of the EPR signal of the sulfide-bridged double cubane is observed; this indicates that the electron is likely in a trapped state in one of the clusters and does not fluctuate between the two (at least not at the temperatures used for the EPR measurements). The observed variation in EPR intensity could indicate a population of a low-lying excited state, potentially with the same $S = 1/2$ or a larger total spin of $S = 3/2$ and a different relaxation behavior. In the latter case, large zero-field splitting, such that only the $|M_S\rangle = \pm 1/2$ doublet is thermally occupied, could then explain the experimental observations. In this respect, note that an $S = 3/2$ ground state has been observed for a number of one-electron-reduced single-cubane clusters.[1a,16] Further experiments are required to investigate the interesting properties of the one-electron-reduced double cubane in detail.

Conclusions

In this study, we report the preparation of three new *para*-pyridylthiolate-ligated iron–sulfur cubane clusters. The single clusters $(Bu_4N)_2[Fe_4S_4(SMePy)_4]$ and $(Bu_4N)_2[Fe_4S_4(SPy)_4]$ are notable additions to the archive of synthetic [4Fe–4S] cubane clusters with similar syntheses and geometric and electronic properties. Most interesting is the isolation of the sulfide-bridged double cubane $(Bu_4N)_4[\{Fe_4S_4(SPy)_3\}_2S]$, which is intentionally formed with the addition of sulfide ions to the cluster synthesis and also through cluster decomposition and solution equilibrium with the single cluster $(Bu_4N)_2[Fe_4S_4(SPy)_4]$. As the single cluster $(Bu_4N)_2[Fe_4S_4(SMePy)_4]$ does not readily form sulfide-bridged double cubanes under the same conditions, it can be inferred that the tautomerization of the 4-pyridinethiolato ligand is the likely origin of the propensity of the single cluster to lose sulfide ions in a decomposition pathway, which is somehow stabilized or initiated by the 4-pyridinethiolato ligand. Hence, $(Bu_4N)_4[\{Fe_4S_4(SPy)_3\}_2S]$ is the first example of a sulfide-bridged all-thiolate ligated cluster that has been structurally characterized in the absence of a large encapsulating ligand. Although the equilibrium of single and double clusters makes the crystallization and isolation of the pure complexes difficult, we succeeded in isolating both species in the form of single crystals and were able to determine their crystal structures. The structures of the 4-pyridinethiolato-ligated single cluster and the sulfide-bridged double cluster show typical internal and external Fe–S bond lengths within 2.2–2.4 Å, and reduction potentials that are more positive than those of the analogous phenylthiolato-ligated clusters. The unique spectroscopic features in the ^{1}H NMR and far-IR spectra of the single and sulfide-bridged double cubane clusters allow for a simple check of the purity of the collected crystalline material. One-electron reduction of the single and double 4-
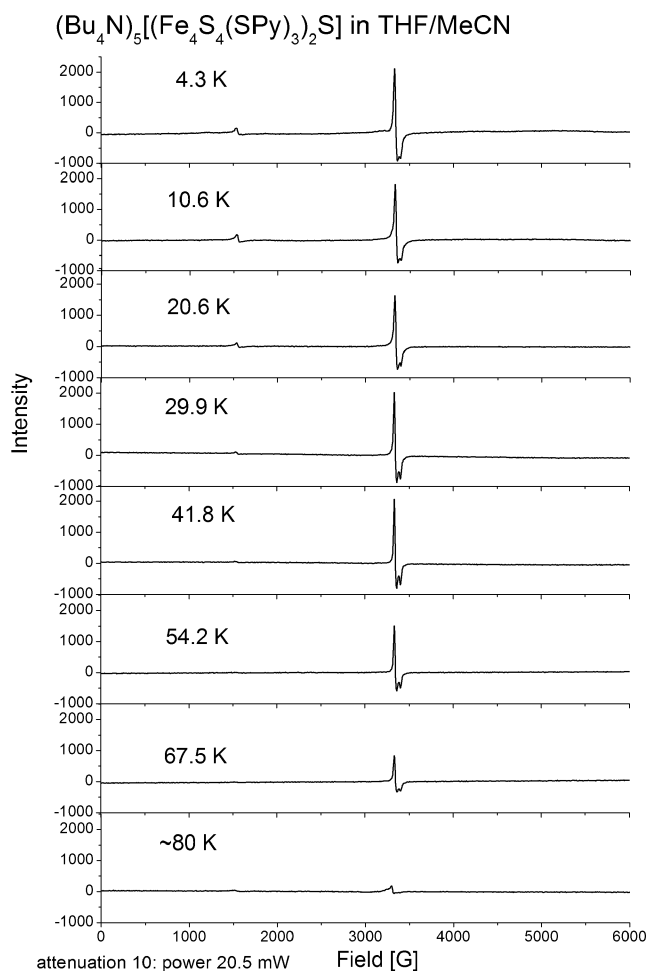

$(Bu_4N)_5[(Fe_4S_4(SPy)_3)_2S]$ in THF/MeCN

attenuation 10: power 20.5 mW

Figure 8. EPR spectra for the one-electron-reduced cluster $(Bu_4N)_5$-$[\{Fe_4S_4(SPy)_3\}_2S]$ at varying temperatures (see also Figure S15).

pyridinethiolato-ligated clusters $(Bu_4N)_2[Fe_4S_4(SPy)_4]$ and $(Bu_4N)_4[\{Fe_4S_4(SPy)_3\}_2S]$ results in the appearance of $g \approx 2$ signals (indicative of $S = 1/2$ ground states) in the EPR spectra of both of these species. The temperature-dependent EPR data of the reduced sulfide-bridged double cubane do not show any broadening of the signal at higher temperature, which suggests that the additional electron is trapped in one of the clusters in the dimer and does not fluctuate at the experimental temperatures. The temperature dependence of the EPR intensity of this species is quite unusual and suggests the presence of a low-lying excited state, but this point requires further study.

The added pyridyl groups of the iron–sulfur clusters prepared here allow for a wide range of interesting applications for these clusters. In particular, the pyridine ligands are open for coordination to an external metal center to form an electron bridge.[17] The clusters have essentially reversible redox cycles in which an electron can be transferred through the aromatic *para*-pyridylthiolate ligands to or from the external metal center. With the abundance of bridging pyridylthiolate ligands for each cluster, materials with three-dimensional linked structures could possibly be obtained with interesting redox and optical properties for use as, for example, conducting solids or materials with nonlinear optical properties. Work towards these goals will be pursued in the future.

Experimental Section

General Procedures: All cluster syntheses were performed under a nitrogen atmosphere in a glove box and by utilizing common Schlenk line techniques. ^{1}H NMR spectra were acquired with a Varian MR400 400 MHz spectrometer and are referenced to solvent signals. Mid-IR spectra were collected with a Perkin–Elmer Spectrum BX FTIR spectrometer, and far-IR data were obtained with a Nicolet 740 FTIR spectrometer with samples as KBr pellets. Elemental analyses were performed by Atlantic Mircolab, Inc., Norcross, GA. Electronic spectra were measured with a Varian CARY 1E UV/Vis spectrometer. Cyclic voltammetry experiments were conducted in 0.1 M solutions of Bu_4NPF_6 in acetonitrile (MeCN) with a glassy carbon working electrode, a Pt counter electrode, and a Ag/AgCl reference electrode with an EG&G Princeton Potentiostat/Galvanostat model 263A. The redox potentials are calibrated to ferrocene/ferrocenium (Fc/Fc$^+$) and reported vs. NHE. EPR spectra were collected with a Bruker X-Band EMX electron spin resonance spectrometer equipped with a Varian liquid nitrogen cryostat (at approximately 80 K) and with an Oxford Instruments liquid-helium cryostat (at 4–65 K). EPR spectra were collected on frozen solutions, using 20 mW microwave power and 100 kHz field modulation with the amplitude set to 1 G.

Materials: All solvents were purified by distillation and degassed. All reagents were used as purchased. $(Bu_4N)_2[Fe_4S_4(SEt)_4]$ was prepared according to published procedures.[4a]

4-Pyridinemethanethiol (PyMeSH): Previously reported syntheses were modified as described in the following.[18] 4-Pyridinemethanechloride hydrochloride (5.00 g, 30.5 mmol) was dissolved in MeOH (30 mL) and heated to reflux while stirring in a round-bottomed flask equipped with a reflux condenser and a slow addition

funnel loaded with thiourea (5.80 g, 76.2 mmol) dissolved in MeOH (100 mL). The thiourea solution was added dropwise to the reaction mixture under reflux. After the addition was complete, the solution was heated to reflux for an additional 1.5–2 h. The solution was cooled to room temperature, and the volume of solvent was reduced under vacuum until a precipitate was observed. The resulting concentrated solution was cooled to –10 °C overnight. The resulting beige precipitate was collected by suction filtration, washed with cold MeOH, and dried under vacuum over P_2O_5. The filtrate volume was reduced, and the solution was cooled again to afford additional collections of solid 4-methylpyridineisothiouronium chloride for a total yield of 4.93 g (82%).

The thiouronium salt (2.5 g, 12.3 mmol) was dissolved in deionized (DI) water (50 mL), and excess solid $NaBH_4$ (2.3 g, 60.8 mmol) was added slowly with stirring. The solution was stirred for 30 min and then acidified with 6 M HCl until a pH of 6 was reached (and maintained). The resulting thiol was extracted with $CHCl_3$ (70 mL × 4), washed with DI water, and dried with Na_2SO_4. The solvent was then removed under vacuum to afford a smelly yellow oil (2.6 g, 83%). ^{1}H NMR (400 MHz, CD$_3$OD, room temp.): $\delta = 8.45$ (d, 2 H), 7.43 (d, 2 H), 3.74 (s, 2 H, CH$_2$) ppm.

$(Bu_4N)_2[Fe_4S_4(SPy)_4]$: $(Bu_4N)_2[Fe_4S_4(SEt)_4]$ (0.88 g, 0.81 mmol) was dissolved in MeCN (30 mL), and the solution was stirred in a glove box. Solid 4-pyridinethiol (PySH, 0.45 g, 4.05 mmol) was added to the solution, and the flask was sealed and evacuated. The reaction mixture was allowed to stir under static vacuum for 1 h. The resulting solution was filtered through a medium frit. The filtrate was layered with Et$_2$O (100 mL) to diffuse overnight. The resulting black solid was a mixture of crystals and amorphous solid and was collected by suction filtration, washed with Et$_2$O (5 mL), and dried under vacuum. ^{1}H NMR analysis indicated that the bulk of the resulting solid was $(Bu_4N)_2[Fe_4S_4(SPy)_4]$ and $(Bu_4N)_4$-$[\{Fe_4S_4(SPy)_3\}_2S]$ in a ratio of 12:1. The resulting solid mixture was recrystallized several times from MeCN solution and layered with Et$_2$O until discernible black cubic crystals were collected. ^{1}H NMR (400 MHz, CD$_3$CN, room temp.): SPy: $\delta = 8.96$ (s), 5.92 (br. s); Bu_4N^+: 3.10 (br. m, 16 H), 1.63 (br. m, 16 H), 1.36 (br. m, 16 H), 0.98 (br. m, 24 H) ppm; see Figure S6. FTIR (KBr): $\tilde{\nu} = 2958$ (m), 2871 (m), 1567 (s), 1527 (w), 1475 (s), 1405 (w), 1378 (w), 1261 (w), 1213 (w), 1099 (m), 1062 (w), 1025 (w), 982 (w), 875 (w), 803 (m), 703 (s), 495 (w), 426 (w), 357 (w) cm^{-1}; see Figure S4. CV (MeCN, 0.01 M): –401.2 mV $[Fe_4S_4]^{2+/1+}$; see Figure S5. $C_{52}H_{88}Fe_4N_6S_8$ (1277.18): calcd. C 48.90, H 6.90, N 6.60, S 20.10; found C 48.82, H 6.84, N 6.48, S 20.24.

$(Bu_4N)_2[Fe_4S_4(SMePy)_4]$: $(Bu_4N)_2[Fe_4S_4(SEt)_4]$ (0.44 g, 0.41 mmol) was dissolved in MeCN (20 mL), and the oil PyMeSH (0.26 g, 2.1 mmol) was added by syringe while stirring in a glove box. The reaction vessel was sealed and a vacuum was applied. The reaction was allowed to stir for 3 h under static vacuum. The reaction mixture was filtered, and the filtrate was layered with Et$_2$O (100 mL). The black precipitate was collected by vacuum filtration, washed with diethyl ether, and dried under vacuum to yield 0.43 g of a black solid product (79%). ^{1}H NMR (400 MHz, CD$_3$CN, room temp.): SMePy: $\delta = 13.29$ (br. s, CH$_2$S), 8.50 (br. s), 7.55 (br. s), Bu_4N^+: 3.05, 1.58, 1.35, 0.95 ppm; see Figure S3. FTIR (KBr): $\tilde{\nu}$ = 2961 (m), 2870 (w), 1596 (m), 1557 (w), 1480 (m), 1409 (m), 1380 (w), 1261 (s), 1203 (w), 1098 (br. s), 1023 (br. s), 990 (m), 869 (m), 736 (w), 687 (w), 561 (w), 483 (w), 424 (w), 356 (w) cm^{-1}; see Figure S1. CV (MeCN, 0.01 M): –742 $[Fe_4S_4]^{2+/1+}$ and –1459 mV $[Fe_4S_4]^{1+/0}$; see Figure S2.

$(Bu_4N)_4[\{Fe_4S_4(SPy)_3\}_2S]$: $(Bu_4N)_2[Fe_4S_4(SEt)_4]$ (0.44 g, 0.41 mmol) was dissolved in MeCN (30 mL), and solid PySH

(0.27 g, 2.43 mmol) and Na_2S (0.03 g, 0.38 mmol) were added while stirring in a glove box. The reaction vessel was sealed, and a vacuum was applied. The reaction was allowed to stir for 24 h under static vacuum. The reaction mixture was filtered, and the filtrate was layered with Et_2O (100 mL). The resulting black solid was a mixture of crystals and amorphous solid and was collected by suction filtration, washed with Et_2O (5 mL), and dried under vacuum. ^1H NMR analysis indicated that the bulk of the resulting solid was $(Bu_4N)_4[\{Fe_4S_4(SPy)_3\}_2S]$ and $(Bu_4N)_2[Fe_4S_4(SPy)_4]$ in a ratio of 5:1 or better. The resulting solid mixture was recrystallized several times from MeCN solution and layered with Et_2O until discernible black rodlike crystals were collected. Often the crystals were accompanied by other solid material and manual separation was necessary to collect pure product. ^1H NMR (400 MHz, CD_3CN, room temp.): SPy: δ = 9.15 (br. s), 5.13 (br. s), Bu_4N^+: 3.09, 1.64, 1.37, 0.97 ppm; see Figure S9. FTIR (KBr): $\tilde{\nu}$ = 2955 (m), 2869 (m), 1567 (s), 1524 (w), 1474 (s), 1403 (m), 1377 (m), 1309 (w), 1261 (w), 1214 (w), 1100 (m), 1062 (w), 1022 (w), 981 (m), 876 (w), 803 (s), 704 (s), 495 (m), 427 (w), 367 (w) cm^{-1}; see Figure S7. CV (MeCN, 0.01 M): $E_{1/2}$ = –528 mV $[(Fe_4S_4)_2S]^{4+/3+}$; E_{pc} = –828 $[(Fe_4S_4)_2S]^{3+/2+}$, ca. –1050 $[(Fe_4S_4)_2S]^{2+/1+}$, ca. –1370 mV $[(Fe_4S_4)_2S]^{1+/0}$; see Figure S8. $C_{94}H_{168}Fe_8N_{10}S_{15}$ (2366.10): calcd. C 47.70, H 7.20, N 5.90, S 20.30; found C 47.13, H 7.11, N 5.91, S 20.47.

Structure Determination of $(Bu_4N)_2[Fe_4S_4(SPy)_4]$ and $(Bu_4N)_4-[\{Fe_4S_4(SPy)_3\}_2S]$: Black needles of $(Bu_4N)_4[\{Fe_4S_4(SPy)_3\}_2S]$ were grown by layering Et_2O over a MeCN solution of the compound at room temperature. A crystal of dimensions $0.47 \times 0.22 \times 0.005$ mm was mounted on a Bruker SMART APEX-I CCD-based X-ray diffractometer equipped with a low-temperature device and fine focus Mo-target X-ray tube (λ = 0.71073 Å) operated at 1500 W (50 kV, 30 mA). The X-ray intensities were measured at 85(1) K; the detector was placed at a distance of 5.055 cm from the crystal. A total of 2220 frames were collected with a scan width of 0.5° in ω and 0.45° in ϕ with an exposure time of 75 s/frame. The integration of the data yielded a total of 164432 reflections to a maximum 2θ value of 48.78°, of which 18681 were independent and 12528 were greater than $2\sigma(I)$. The final cell constants (Table S1) were based on the *xyz* centroids of 9849 reflections above $10\sigma(I)$. Analysis of the data showed that the crystal exhibited negligible decay during data collection; the data were processed with SADABS and corrected for absorption. The structure was solved and refined with the Bruker SHELXTL (version 2008/4) software package with Z = 4 for the formula $C_{94}H_{168}N_{10}S_{15}Fe_8$. All non-hydrogen atoms were refined anisotropically with the hydrogen atoms placed in idealized positions. Full-matrix least-squares refinement based on F^2 converged at $R1$ = 0.0562 and $wR2$ = 0.1280 [based on $I > 2\sigma(I)$] and $R1$ = 0.1009 and $wR2$ = 0.1476 for all data. Additional details are presented in Table S1 and are given in the Supporting Information.

Reduction of $(Bu_4N)_2[Fe_4S_4(SPy)_4]$ and $(Bu_4N)_4[\{Fe_4S_4(SPy)_3\}_2-S]$:[19] Solid $(Bu_4N)_2[Fe_4S_4(SPy)_4]$ (5.4 mg, 0.00423 mmol) and $(Bu_4N)_4[\{Fe_4S_4(SPy)_3\}_2S]$ (9.8 mg, 0.00414 mmol) were deposited into two separate 2 mL volumetric flasks. A stock solution of the reductant Na·acenaphthylene (36 mM) was prepared in a 10 mL volumetric flask by dissolving acenaphthylene (65.1 mg, 0.428 mmol) in tetrahydrofuran (THF, ca. 6 mL), adding Na metal (8.3 mg, 0.361 mmol), diluting to 10 mL with THF, and letting the suspension stir for several hours. A stock solution of Bu_4NBr (8.31 mM) was prepared by dissolving Bu_4NBr (13.4 mg, 0.0416 mmol) in a THF/MeCN (ca. 4:1) mixture in a 5 mL volumetric flask. Each cluster was dissolved in MeCN (0.3 mL) in the volumetric flask, to which the Bu_4NBr solution (8.31 mM, 0.5 mL) and the Na·acenaphthylene solution (36 mM, 0.12 mL) were added.

The resulting solutions were shaken and left for 20 min. The resulting dark solutions were then filtered through Celite, and an insignificant amount of black precipitate was collected. The resulting filtrate was loaded into quartz EPR tubes, sealed, and frozen for EPR spectroscopy.

CCDC-947515 contains the supplementary crystallographic data for this paper. These data can be obtained free of charge from The Cambridge Crystallographic Data Centre via www.ccdc.cam.ac.uk/data_request/cif.

Supporting Information (see footnote on the first page of this article): Spectroscopic characterization of $(Bu_4N)_2[Fe_4S_4(SPy)_4]$, $(Bu_4N)_2[Fe_4S_4(SMePy)_4]$, and $(Bu_4N)_4[\{Fe_4S_4(SPy)_3\}_2S]$, additional unit-cell packing diagrams, and crystallographic data.

Acknowledgments

[1] a) R. Holm, P. Kennepohl, E. I. Solomon, *Chem. Rev.* **1996**, *96*, 2239–2314; b) P. A. Frey, G. H. Reed, *ACS Chem. Biol.* **2012**, *7*, 1477–1481.

[2] P. V. Rao, R. H. Holm, *Chem. Rev.* **2004**, *104*, 527–559.

[3] A. Dey, F. E. Jenney Jr., M. W. W. Adams, E. Babini, Y. Takahashi, K. Fukuyama, K. O. Hodgson, B. Hedman, E. I. Solomon, *Science* **2007**, *318*, 1464–1468.

[4] a) B. A. Averill, T. Herskovitz, R. H. Holm, J. A. Ibers, *J. Am. Chem. Soc.* **1973**, *95*, 3523–3534; b) H. Beinert, R. H. Holm, E. Münck, *Science* **1997**, *277*, 653–659.

[5] a) W. E. Cleland, D. A. Holtman, M. Sabat, J. A. Ibers, G. C. DeFotis, B. A. Averill, *J. Am. Chem. Soc.* **1983**, *105*, 6021–6031; b) C. Zhou, R. H. Holm, *Inorg. Chem.* **1997**, *36*, 4066–4077.

[6] W. Lo, P. Zhang, C.-C. Ling, S. Huang, R. H. Holm, *Inorg. Chem.* **2012**, *51*, 9883–9892.

[7] a) T. Mochida, M. Ueda, H. Moriyama, *Mol. Cryst. Liq. Cryst.* **2000**, *342*, 91–06; b) M. Ueda, T. Mochida, *Inorg. Chim. Acta* **2003**, *353*, 306–309.

[8] a) Y. Zhang, J. Zuo, H. Zhou, R. H. Holm, *J. Am. Chem. Soc.* **2002**, *124*, 14292–14293; b) Y. Ohki, M. Imada, A. Murat, Y. O. Sunada, S. Honda, M. T. Sasamori, N. Tokitoh, M. Katada, K. Tatsumi, *J. Am. Chem. Soc.* **2009**, *131*, 13168–13178.

[9] a) T. D. P. Stack, M. J. Carney, R. H. Holm, *J. Am. Chem. Soc.* **1989**, *111*, 1670–1676; b) P. R. Challen, S.-M. Koo, W. R. Dunham, D. Coucouvanis, *J. Am. Chem. Soc.* **1990**, *112*, 2455–2456; c) J. A. Weigel, R. H. Holm, *J. Am. Chem. Soc.* **1991**, *113*, 4184–4191; d) T. Terada, T. Wakimoto, T. Nakamura, K. Hirabayashi, K. Tanaka, J. Li, T. Matsumoto, K. Tatsumi, *Chem. Asian J.* **2012**, *7*, 920–929; e) J. Huang, S. Mukerjee, B. M. Segal, H. Akashi, J. Zhou, R. H. Holm, *J. Am. Chem. Soc.* **1997**, *119*, 8662–8674; f) M. A. Whitener, G. Peng, R. H. Holm, *Inorg. Chem.* **1991**, *30*, 2411–2417.

[10] a) R. A. Jones, A. R. Katritzky, *J. Chem. Soc.* **1958**, 3610–3613; b) S. Stoyanov, I. Petkov, L. Antonov, T. Stoyanova, P. Karagiannidis, P. Aslanidis, *Can. J. Chem.* **1990**, *68*, 1482–1489.

[11] P. R. Challen, Ph. D. Thesis, University of Michigan, Ann Arbor, **1990**.

[12] Y. Kim, J. Han, *Bull. Korean Chem. Soc.* **2012**, *33*, 48–54.

[13] a) L. Guodong, Z. Hongtu, H. Sheng-Zhi, T. C. W. Mak, *Acta Crystallogr., Sect. C* **1987**, *43*, 352–353; b) J. Gloux, P. Gloux, H. Hendriks, G. Rius, *J. Am. Chem. Soc.* **1987**, *109*, 3220–3224.

[14] C. Zhou, J. W. Raebiger, B. M. Segal, R. H. Holm, *Inorg. Chim. Acta* **2000**, *300–302*, 892–902.

FULL PAPER

[15] T. Herskovitz, B. A. Averill, R. H. Holm, J. A. Ibers, W. D. Phillips, J. F. Weiher, *Proc. Natl. Acad. Sci. USA* **1972**, *69*, 2437–2441.

[16] P. A. Lindahl, E. P. Day, T. A. Kent, W. H. Orme-Johnson, E. Münck, *J. Biol. Chem.* **1985**, *260*, 11160–11173.

[17] D. L. Gerlach, D. Coucouvanis, N. Lehnert, *Eur. J. Inorg. Chem.* **2013**, 3883–3890.

[18] a) J. H. Barnes, M. Fatome, C. E. L. Jones, S. G. Murray, *Eur. J. Med. Chem.* **1988**, *23*, 211–216; b) D. Mascagna, M. d'Ischia, C. Costantini, G. Prota, *Synth. Commun.* **1994**, *24*, 35–42.

[19] C. J. A. Daley, R. H. Holm, *J. Inorg. Biochem.* **2003**, *97*, 287–298.

5264